RESEARCH PAPER

Pressure-Shear Plate Impact Investigation of Dynamic Shearing Resistance of Polycrystalline Pure Magnesium at Elevated Temperatures: Twinning and Dislocation-Slip Rates

T. Wang[1] · V. Prakash[2]

Abstract

Polycrystalline magnesium (Mg) and its alloys have been widely investigated in order to better understand and improve their mechanical properties. However, significant questions remain as to how these materials behave under ultra–high strain-rate loading conditions, especially at elevated temperatures. In view of this, in the present study, elevated temperature combined pressure–and–shear plate impact experiments are employed to investigate the dynamic shearing resistance of polycrystalline commercially pure (99.9%) magnesium at strain-rates in excess of 10^5 s^{-1}, temperatures up to 500 °C, and shear strains > 100%. The results of the study provide important insights into the shearing resistance of polycrystalline pure Mg under extreme thermomechanical loading conditions and its relationship to the evolution of various inelastic deformation modes – dislocation-mediated slip, deformation twinning, and geometric strain softening – with different mechanisms becoming dominant at different levels of inelastic strains and test temperatures.

Introduction

Magnesium has a hexagonal close–packed (hcp) crystal structure, which exhibits significant anisotropic mechanical properties when compared to the higher symmetry face-centered cubic (fcc) and body-centered cubic (bcc) crystalline materials. The large anisotropy in the mechanical properties of Mg can be attributed to the very different Critical Resolved Shear Stress (CRSS) of the available slip and twinning modes [1, 2], which are understood to be sensitive to both temperature [3, 4] and strain-rates [5, 6].

At room temperature, plastic deformation in hcp crystals is understood to depend on the c/a ratio. For hcp crystals with an axis ratio $c/a \geq 1.63$, the most densely packed planes and directions are the (0001) basal plane and the three <1120> directions. For crystals with $c/a < 1.63$, the basal plane is not the most densely packed plane anymore, but comparable to the prism and pyramidal planes. In this case slip can also occur on the prism and pyramidal planes, and, correspondingly, many more slip systems are likely to be activated. Polycrystalline Mg has a near optimum c/a ratio of ~ 1.624. Consequently, plastic slip can be accommodated by easy glide of dislocations along the basal, prismatic and pyramidal planes in the $11\bar{2}0$ directions, commonly referred to as the *a* type slip systems. However, to accommodate compatible plastic strains, a non *a* type slip system must also be activated. Accordingly, despite their relatively higher CRSS levels, the *c*-prismatic and *c* + *a*-pyramidal slip systems are also activated to accommodate strains along the c-axis [7, 8].

Along with dislocation mediated slip, deformation twinning is understood to be an important deformation mechanism in hcp lattice structures, especially at high strain-rates and low temperatures, where it has been found to be more prevalent [9]. In general, the three types of twinning modes that are expected in Mg include extension twinning, contraction twinning, and double twinning [10–13].

Table 1 summarizes the most commonly observed < a > and < c + a > type dislocation slip systems along with the extensional and contraction deformation-twinning modes for hcp-Mg. Also shown in Table 1 are their corresponding CRSS levels, estimated at room temperature and quasi-static loading conditions [14].

✉ V. Prakash
vikas.prakash@wsu.edu

[1] Department of Mechanical and Aerospace Engineering, Case Western Reserve University, Cleveland, OH 44106, USA

[2] Institute for Shock Physics, Washington State University, Pullman, WA 99164, USA

Table 1 Summary of the commonly observed $<a>$ and $<c+a>$ type dislocation slip systems along with the extensional and contraction deformation twinning modes. The corresponding CRSS range at room temperature and quasi-static strain rates for each of these deformation modes is provided in Column 5 [14]

Dislocation slip and deformation twinning modes	Slip/twin plane	Slip/twin direction	Number of slip/twin systems	CRSS at RT and quasi-static strain rates (MPa)
$<a>$ Basal slip	$\{0001\}$	$(11\bar{2}0)$	3	0.5
$<a>$ Prismatic slip	$\{1\bar{1}00\}$	$(11\bar{2}0)$	3	10 to 45
$<a>$ Pyramidal slip	$\{1 0\bar{1}1\}$	$(11\bar{2}0)$	6	10 to 45
$<c+a>$ Pyramidal I & II slip	$\{11\bar{2}2\}$	$(11\bar{2}3)$	6	35 to 80
Extension Twinning	$\{10\bar{1}2\}$	$(10\bar{1}0)$	6	2 to 5
Contraction Twinning	$\{10\bar{1}1\}$	$(10\bar{1}2)$	6	30 to100

Since polycrystalline Mg exhibits strong plastic flow anisotropy, classical plasticity theories developed for isotropic materials are generally not applicable in the description of their inelastic behavior. Also, since strain hardening of flow stress in Mg is understood to be different in the presence of twinning (than with just dislocation slip) [15], the shape of the measured stress–strain curves can provide important insights into the dominant deformation mechanism(s). Accordingly, extension twinning dominant deformations exhibit a clear sigmoidal shape in their stress–strain curves with only a modest dependence of flow stress on strain hardening and temperature, whereas slip-dominated deformations show more consistent strain hardening [14]. Also, since extension twinning leads to lattice reorientation within the parent grain, within the twinned region $c + a$ – pyramidal slip can become the major deformation mechanism along with a – basal slip as the minor. At the exhaustion of extension twinning, an increase in local strain hardening rate and temperature sensitivity is expected, giving rise to a sigmoidal shape to the stress vs strain curve. On the other hand, for orientations where contraction twinning is favorable, the stress–strain curves exhibit a spike at the onset of plastic deformation followed by a decrease in flow stress with further straining [14]. The latter can be attributed to the activation of relatively low CRSS slip mechanisms, e.g., basal slip, within the previously twinned region.

The temperature dependence of CRSS for the various dislocation slip modes in pure Mg has been investigated in the quasi-static strain-rate regime [3, 4]. In the temperature range from room to 500 °C the a type basal slip has been found to be nearly independent of temperature; however, a lower CRSS for a prismatic slip and $c + a$ pyramidal slip has been reported as the sample temperatures are increased. Furthermore, twin-slip interactions can contribute to additional slip hardening with the introduction of twin boundaries, which can act as further barriers to dislocation slip. Also, it has been postulated [16, 17], that at strain-rates in excess of 5×10^4 s^{-1} and elevated temperatures, inelastic deformation can be controlled by mechanisms other than thermal activation, such as viscous (phonon) drag, which can considerably increase the resistance to dislocation slip, and consequently the material strength in pure metals.

The work presented in this paper is motivated by our recent developments in experimental capabilities which allows dynamic shearing resistance of engineering materials to be investigated at extreme thermo-mechanical deformation states [18, 19]. Using these new capabilities, in the present study, we have conducted elevated temperature combined pressure–and–shear plate impact (PSPI) experiments on polycrystalline, commercially pure Mg to investigate its dynamic shearing resistance at strain-rates in excess of 10^5 s^{-1}, temperatures up to ~500 °C, and shear strains > 100%. Understanding material behavior of hcp-Mg at elevated temperatures and very high strain rates is particularly valuable since both slip and twinning deformation mechanisms are expected to involve evolving material microstructures/textures as deformation precedes with different mechanisms becoming dominant at different levels of inelastic strains, and also for immediate contribution to improved high-temperature constitutive models for hcp metals as they approach their melt points at ultra–high shearing rates.

Experimental Technique: Elevated Temperature Pressure–Shear Plate Impact

The combined pressure–shear plate impact experiment (PSPI) is a well-established technique for evaluating dynamic shearing resistance of metals at ultra–high shear strain rates (between 10^5 and 10^7/s) [20–23]. In the present study a novel modification of the PSPI technique, which allows these experiments to be conducted at elevated temperatures, was employed [24]. A schematic of the experimental configuration [25–28], is shown in Fig. 1. The flyer plate assembly is modified to include a thin metal foil specimen diffusion bonded to a (high hardness and

high impedance) pure (99.9%) tungsten carbide flyer plate. The rear–end of the sabot holds a sealing O-ring and a Teflon key, which slides in the keyway of the gun barrel to prevent rotation of the sabot during its acceleration. To conduct the elevated temperature PSPI experiment the sample, held at the front end of a custom heat-resistant sabot, is heated to the desired temperature by radiation using a non-contact 800 W resistive coil heater located at the breech end of the gun barrel. During the experiment, the temperature of the sample is monitored continuously using a K-type thermocouple probe attached directly to the sample. Once the desired test temperature is reached, the sabot is accelerated down the gun-barrel by means of compressed nitrogen gas to impact a stationary target plate in the impact chamber, resulting in combined pressure–and–shear loading of the thin Mg foil sample. It is to be noted that in these experiments the error in the reported sample temperatures are less than 5 °C. During acceleration of the sabot down the gun barrel (length ~ 3 m) the sample can lose heat to the surrounding by three modes – conduction, convection and radiation. Since the flyer plate is supported on an aluminum silicate baseplate (thermal conductivity ~ 2 W/m–K) at the front of the sabot, and the sabot accelerates down the gun barrel in a rough vacuum (~ 60 mm of Hg), we can rule out any appreciable heat loss from the heated flyer plate to its surroundings by either conduction and/or convection heat transfer modes. The only other viable heat loss

source is radiation, which again is estimated to be small since the flight time of the sabot down the gun barrel is less than ~ 0.2 s. When conducting these experiments the temperature of the sample on the sabot is set to be just higher than the desired test temperature to compensate for any heat loss to the surroundings.

Because of the relatively large impedance mismatch between the Mg sample and the bounding plates (tungsten carbide), the normal stress in the specimen rings-up to a uniform hydrodynamic compressive state within a few reverberations of the longitudinal wave in the specimen. The shear stress in the specimen also rings up quickly at the arrival of the transverse wave at the specimen plane, enabling the dynamic shearing resistance of the sample to be probed under well-defined stress and strain-rate states up to large plastic shear strains. On the rear surface of the target plate a 500 lines/mm holographic grating is fabricated to enable measurement of combined normal and transverse particle displacement history of the free surface of the target plate by using an all-fiber-optics-based heterodyne combined normal-displacement/transverse-displacement (NDI/TDI) interferometer [29, 30]. A detailed description of the protocols for conducting these experiments can be found in [18].
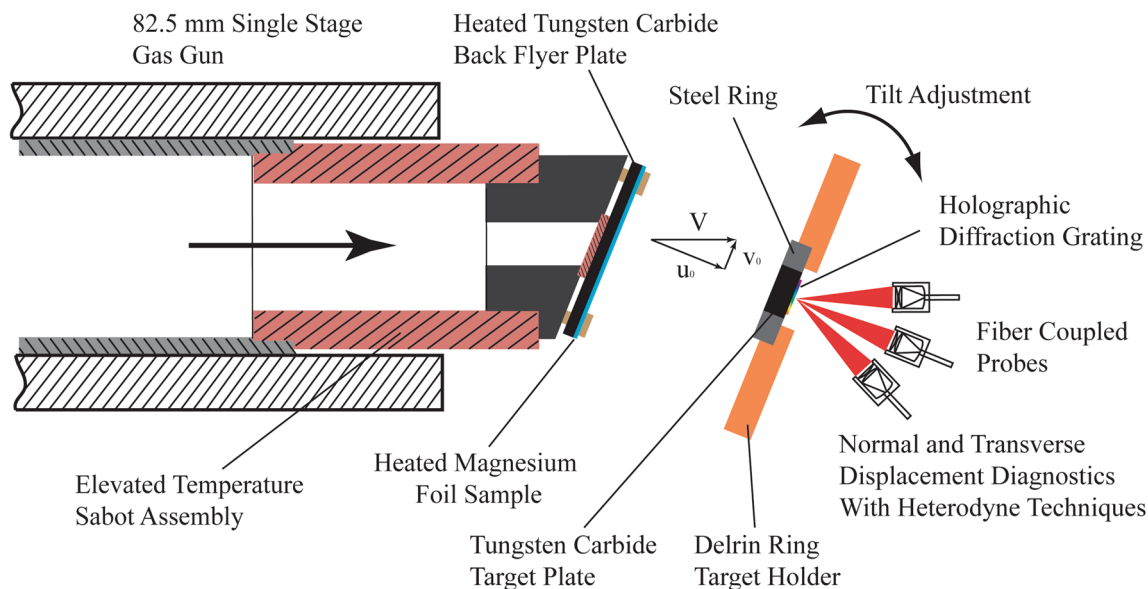

Fig. 1 Schematic of the elevated temperature PSPI experiment. Here, a heated sample is held at the front surface of the flyer plate, which is inclined 22˚ with respect to the direction of travel. The flyer/sample is accelerated down the gun barrel and is made to impact a station-ary target plate forming the PSPI sandwich. Wave histories at the free surface of the target plate are measured with normal and transverse displacement diagnostics

Target Assembly and Sabot

To conduct the elevated temperature PSPI experiments flyer plates of 76.2 mm in diameter and 5.84 mm in thickness, and target plates of 31.75 mm in diameter and 6.35 mm in thickness were fabricated from 99.9% pure tungsten carbide (WC) procured from Research and PVD Materials LLC. Typical elemental composition of the WC plates was 99.9% W with < 500 ppm N, < 300 ppm O, < 200 ppm Fe, < 100 ppm H, < 30 ppm S, and < 20 ppm Al. In addition, elements detected at < 100 ppm sensitivity level were Co, Cr, Mo, and Ni. The (minimum) density of the WC plates was 15.2 g/cm^3. The high dynamic strength [31] (Hugoniot Elastic Limit (HEL) ~ 6GPa) and melting point (~ 3058 °C) of WC ensure that the flyer and target plates remain elastic at the impact velocities and test temperatures of interest to the present study. Three equi-spaced holes of diameter 5 mm were machined on a 62 mm diameter bolt circle on the WC flyer plate to secure it to a sabot using alumina screws. Moreover, six 3 mm diameter holes were drilled on an aluminum ring to house six voltage biased copper pins, which provide the trigger signal for data acquisition, and measurement of flyer/target tilt at impact.

To enable the desired pressure–shear loading on the samples during impact, the Mg foil samples are diffusion bonded to the WC flyer plate using a vacuum hot press. To carry out the diffusion bonding, the WC flyer plate is first thoroughly cleaned with acetone, then with ethanol and lastly with de-ionized water. The chemically cleaned WC flyer plate is baked on a hot plate at 350 °C for ~ 10 min to remove any impurities. The foil sample is then placed on the WC flyer plate and sandwiched between two high-purity fine-grained (~ 1 µm grain size) graphite disks. Next, a compressive stress of ~ 20 MPa is used on the sample-graphite disk assembly while the furnace temperature is increased slowly from room temperature to ~ 430 °C. The assembly is then left in the hot press for 10 h, after which the furnace is turned off and the sample is slowly cooled down to room temperature while maintaining the compressive stress on the assembly. Detailed microstructural analysis of the pre-test samples is provided in the Section on "Experimental Results and Discussion."

Wave Analysis in the Flyer and Target Plates

Wave propagation in the flyer-sample-target assembly is illustrated schematically as a time-distance diagram in Fig. 2. At impact, two stress waves propagate into the target as well as the specimen and the flyer plate: a
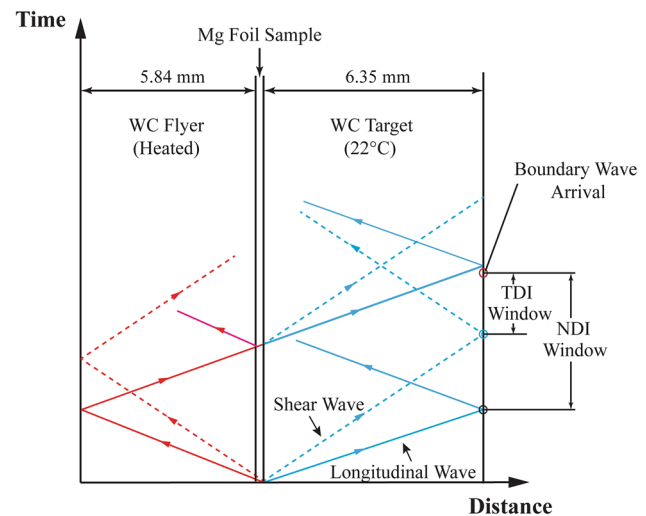

Fig. 2 Time vs. distance diagram used in the analysis of normal and shear loading for a typical combined pressure–shear plate impact experiment. The heated magnesium foil sample, which is diffusion bonded to the impact face of the WC flyer plate, is accelerated down the gun barrel to impact a stationary WC target plate at room temperature. The solid and dashed lines in the figure correspond to the longitudinal and transverse waves, respectively, in the WC flyer and WC target plates at impact. The window times for normal displacement interferometry (NDI) and transverse displacement interferometry (TDI) for the experiment are also shown in the figure

longitudinal wave propagating at the elastic longitudinal wave speed c_1 (represented by solid lines), and a transverse wave propagating at the elastic transverse wave speed c_2 (as represented by the dashed lines). The free-surface particle velocity measurements are made prior to the arrival of release waves at the monitoring point from the lateral boundaries of the target plate assembly. The dimensions of the target and flyer plates are strategically selected to provide a window time of ~ 1 µs for the measurement of the transverse waves and ~ 1.5 µs for the longitudinal waves.

Both flyer and target plates are unstressed initially. The target is at rest while the flyer is carried by the sabot at a velocity, V_o. Using the method of characteristics for 1-D wave propagation in elastic plates along with appropriate boundary and initial conditions, the normal stress, $\sigma_{33}(t)$, and shear stress, $\tau_{23}(t)$,, in the sample can be expressed as

$$\sigma_{33}(t) = -\tfrac{1}{2}Z_{Lt}u_{fs}(t); \tau_{23}(t) = -\tfrac{1}{2}Z_{Tt}v_{fs}(t), \tag{1}$$

where, Z_{Lt} and Z_{Tt} are the elastic longitudinal and transverse impedance of the target plate; and $u_{fs}(t)$ and $v_{fs}(t)$ are the normal and transverse components of the particle velocity measured at the free surface of the target plate. Note that the 3 direction is normal to the impact surface while the 1 and 2 directions define the specimen plane. The plastic shear strain rate, $\dot{\gamma}_{23}(t)$, and shear strain history, $\gamma_{23}(t)$, in the sample can be expressed as

$$\dot{\gamma}_{23}(t) = \frac{1}{h}\left[V_o \sin\theta - \frac{1}{2}\left(\frac{Z_{Tf}(T)+Z_{Tt}}{Z_{Tf}(T)}\right)v_{fs}(t)\right]; \gamma_{23}(t) = \int_0^t \dot{\gamma}_{23}(t)dt.$$
$$(2)$$

In Eq. (2), h is the thickness of the sample in the unde-formed configuration, θ is the skew angle of impact, and $Z_{Tf}(T)$ is the temperature-dependent transverse impedance of the flyer plate. For the WC flyer plates used in the present work, temperature dependence of the transverse impedance of the flyer plate, has been characterized in our previous work [31].

Experimental Results and Discussion

A series of seven elevated temperature PSPI experiments were conducted on polycrystalline 99.9% pure Mg foil samples at ultra-high strain-rates (10^5/s–10^6/s) and initial test temperatures in the range 23 °C to 487 °C. The limit on the highest temperature for Mg is constrained by the vapor pressure of pure Mg foils at ~ 50 mTorr, which is the typical target chamber pressure prior to impact. The experimental conditions (e.g., target plate thickness, sample thickness, angle of inclination, impact velocities, the angle of flyer-target misalignment (tilt) at impact and initial sample temperatures) for each experiment are summarized in Table 2. The experiments were conducted at impact velocities in the range 99 to 103 m/s at a 22 ° skew angle. Under these impact conditions, the WC flyer and target plates remain elastic during the experiment. Select physical properties of the WC flyer and target plates at ambient conditions are provided in Table 3.

For conducting Shots PSPIMG01 to PSPIMG07 100 μm thick Mg foils were utilized. To conduct PSPI experiments with different foil thickness, i.e., Shot PSPIMG01 (with 80 μm), Shots PSPIMG02 and PSPIMG03 (75 μm), Shot PSPIMG04 (50 μm) and Shots PSPIMG05, PSPIMG06, PSPIMG07 (25 μm) ~ 100 μm thick diffusion bonded foils were thinned by appropriate lapping and polishing operations. Also, since Shot PSPIMG07 was conducted at room

Table 3 Select physical properties of 99.9% pure Tungsten Carbide plates at ambient conditions

Material	Density (g/cm³)	Longi-tudinal wave speed (mm/μs)	Shear wave speed (mm/μs)	Longi-tudinal imped-ance (GPa-μs/mm)	Shear impedance (GPa-μs/mm)
99.9% Pure WC	15.4	6.858	4.300	105.61	66.22

temperature, the foil sample was simply securely placed on the WC flyer plate with no diffusion bonding.

Electron Backscatter Diffraction Analysis of the Mg foil Samples

Electron Backscatter Diffraction (EBSD) analysis was conducted on the as received and annealed 100 μm thick Mg foil samples in a direction normal to the foil surface (i.e., along the impact direction). A step size of 2 μm was used to acquire the EBSD images. The corresponding pole figure for the as-received Mg foil is shown in Fig. 3a. A typical rolled texture is observed with the [0001] basal poles aligned with the foil surface normal. To anneal the Mg foil samples the as-received foils were heated for at least 8 h at 450 °C in argon atmosphere and then allowed to cool slowly. The motivation for annealing the foils was to minimize sample to sample variation in foil microstructure due to grain growth/coarsening during diffusion bonding and during the sample heating phase to achieve the desired test temperatures. It is to be noted that to conduct the elevated temperature PSPI experiments the annealed samples are heated inside the gun barrel to the desired test temperatures prior to conducting the experiments. Previous work by the authors [19, 32] on shock compressed Mg samples at elevated temperatures has shown that sample heating results in grain coarsening in the sample microstructure, with larger grains being present at higher

Table 2 Summary of the elevated temperature normal plate impact experiments conducted in the present study on commercial purity magnesium

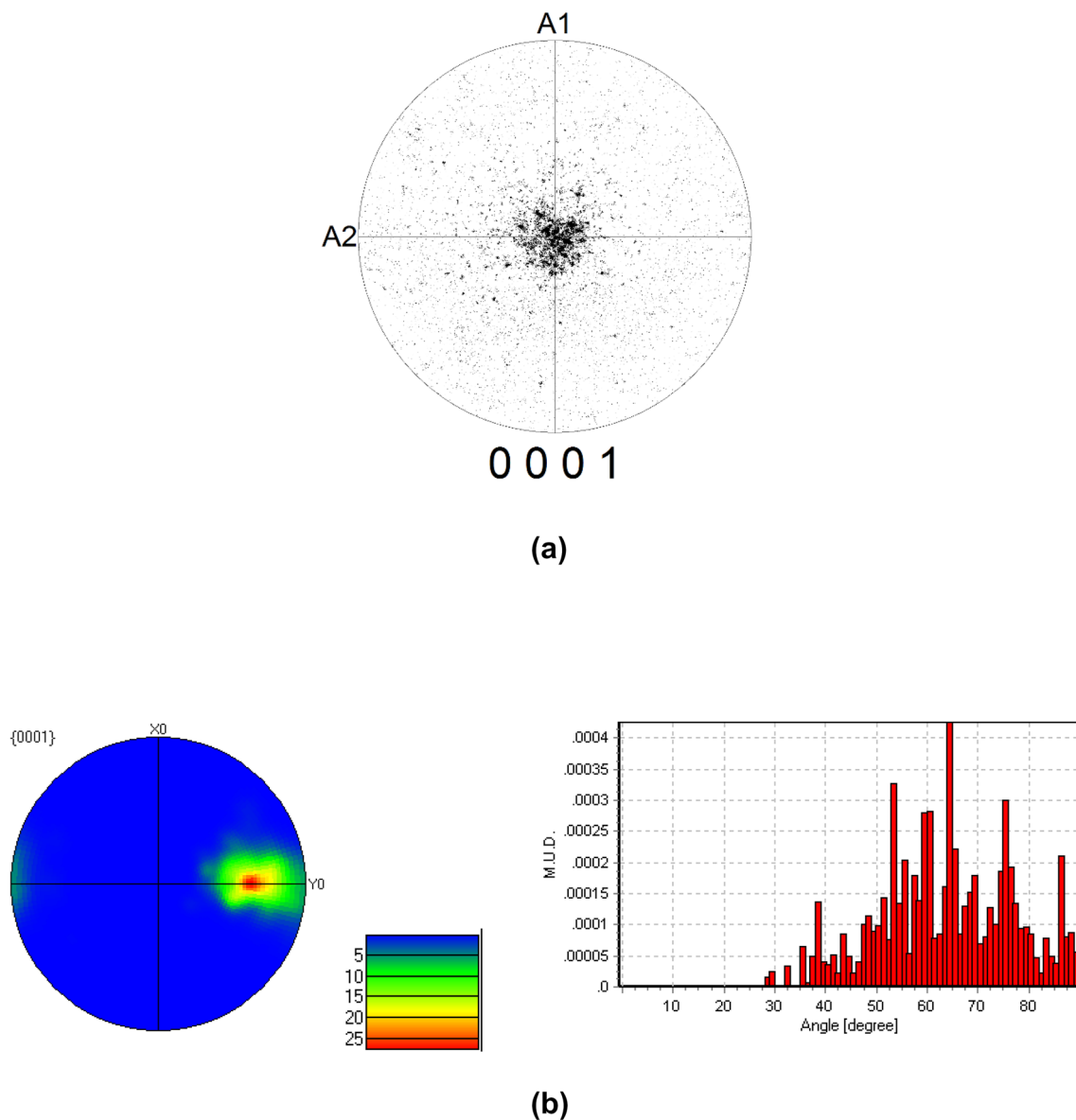| Experiment no	Thickness of the WC target (mm)	Thickness of the Mg Sample (μm)	Angle of inclination (degrees)	Impact velocity (m/s)	Tilt at impact (mrad)	Sample temp (°C)
PSPIMG01	6.3	80	22	103	0.7	23
PSPIMG02	6.3	75	22	100	1.0	205
PSPIMG03	6.3	75	22	103	0.5	305
PSPIMG04	6.3	50	22	100	1.1	487
PSPIMG05	6.3	25	22	100	0.2	390
PSPIMG06	6.3	50	22	101	0.4	23
PSPIMG07	6.3	25	22	99	0.6	23

(a)

(b)

Fig. 3 **a** [0001] pole figures (PF) of the as-received magnesium along the foil surface normal (i.e., along the impact direction). The figure shows that basal poles of the as-received foil are aligned with the foil surface normal. **b** Pole figure (PF) showing that the [0001] basal poles are inclined at an angle of ~ 65 ° respect to the foil surface normal
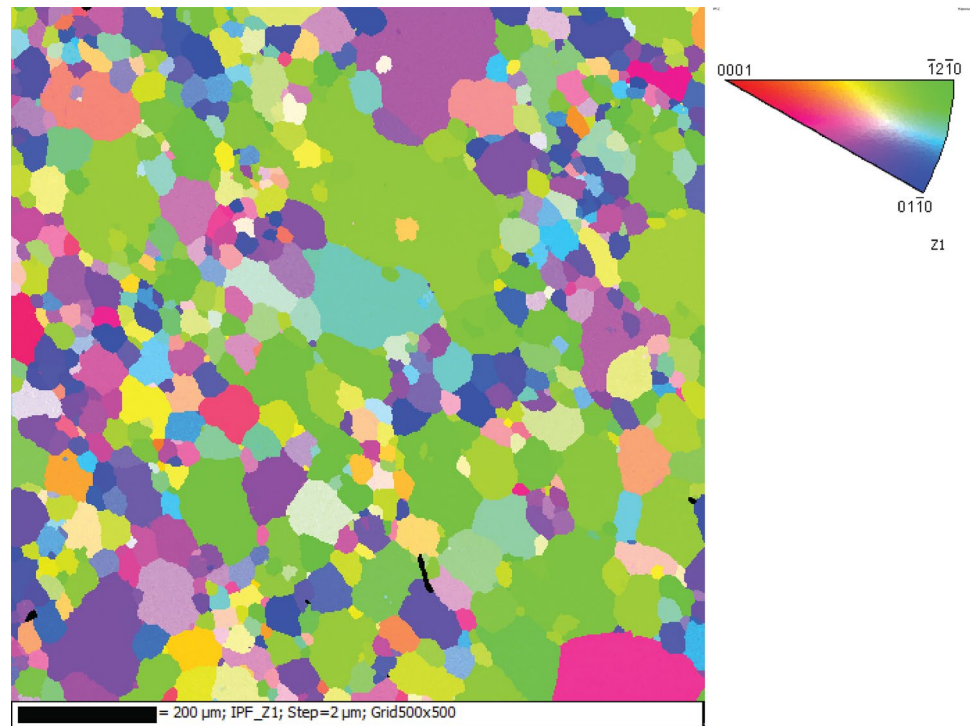
test temperatures. Pre-test annealing helps to mitigate this problem by providing a more uniform material microstructure in the Mg samples at all test temperatures of interest to the present study.

The corresponding pole figure (PF) and grain orientation map (GOM) for the 100 μm thick annealed Mg foil sample are shown in Figs. 3b and 4, respectively. The EBSD data were used to obtain information on material microstructure (texture and grain size) of the foil samples prior to impact. As inferred from the figures, the [0001] basal poles are inclined at an angle of ~ 65 ° respect to the foil surface normal. The weighted area average grain

size for the annealed sample is ~ 37 μm. Also, no deformation twinning is observed in the annealed samples. These 100 μm thick Mg foils were used as samples to conduct the PSPI experiments (Shots PSPIMG01 to PSPIMG06) in the present study.

It should be noted that there are approximately one to three grains across the thickness of the polycrystalline Mg foil samples. Nevertheless, the shearing strength data obtained from these experiments is still representative of sample bulk shearing behavior since the lateral dimension (diameter) of the sample is much larger when compared to the sample grain size (~ 30 mm), and thus there are

large number of grains available for averaging in the sample shearing direction.

Normal and Transverse Particle Velocity Profiles at the Target Free Surface

The normal and transverse free-surface particle velocity profiles obtained from the elevated temperature high-strain-rate PSPI experiments are shown in Figs. 5 and 6, respectively. The abscissa shows the time of arrival of the longitudinal/shear wave at the free surface of the target plate. The solid lines correspond to the room temperature experiments – PSPIMg01, PSPIMg05 and PSPIMg06 conducted on 80 μm, 50 μm and 25 μm thick foil samples, respectively, –- while the dash-dot curves represent the elevated temperature experiments, PSPIMg02, PSPIMg03, PSPIMg05 and PSPIMg04 conducted at 205 °C, 305 °C, 390 °C and 489 °C on 80 μm, 50 μm, 25 μm thick Mg foil samples, respectively. The rise time in the measured normal particle velocity profiles is dictated by the ring-up of the longitudinal waves in the sandwiched sample, which depends on the sample thickness and its wave speed, before reaching a particle velocity plateau governed by the impedance of the heated WC flyer plate and the room temperature WC target plate. The particle velocities at the plateau level, for all the experiments, lie within a narrow range from 92 m/s to 95 m/s, which corresponds to a normal compressive stress $\sigma_{33} \sim 4.6$ GPa.

The free surface transverse particle velocity profiles for the seven PSPI experiments are shown in Fig. 6. Consistent with Fig. 5, the solid lines in Fig. 6 represent the room temperature experiments while the dashed-dot lines represent data obtained from the elevated temperature experiments. The gradual rise (~ 75 ns) in the transverse particle velocity profiles is dictated by the ring-up time of transverse waves in the sample, which is followed by a gradual rise and then a much sharper increase in particle velocity at ~ 600 ns (after the arrival of the shear wave), which are both directly related to the dynamic shearing resistance of the Mg samples. These particle velocity profiles are used along with Eqs. (1) and (2) to obtain the shearing resistance (shear stress) and the plastic shearing rates in the samples, respectively. The shear strains are calculated by taking the integral of the shear strain-rate with time.

Dynamic Shearing Resistance of Polycrystalline Magnesium Foil Samples

In PSPI both normal compression and shear stresses develop in the sample during impact. Accordingly, the stress state in the sample can be expressed as $\boldsymbol{\sigma} = -p(\boldsymbol{e}_1 \otimes \boldsymbol{e}_1 + \boldsymbol{e}_2 \otimes \boldsymbol{e}_2 + \boldsymbol{e}_3 \otimes \boldsymbol{e}_3) + \tau_{23}(\boldsymbol{e}_2 \otimes \boldsymbol{e}_3 + \boldsymbol{e}_3 \otimes \boldsymbol{e}_2)$, where $p = \sigma_{33}$ and is obtained from the normal free surface particle velocity profiles, τ_{23} is the measured shear stress in the sample, and $\boldsymbol{e}_i (i = 1, 2, 3)$ are a set of orthogonal unit vectors. The eigenvalues of the stress tensor

Fig. 5 Normal free-surface particle velocity history for pressure–shear experiments on 99.9% polycrystalline pure magnesium samples. The time axis is shifted to coincide with the arrival of the longituinal wave at the free surface of the target plate
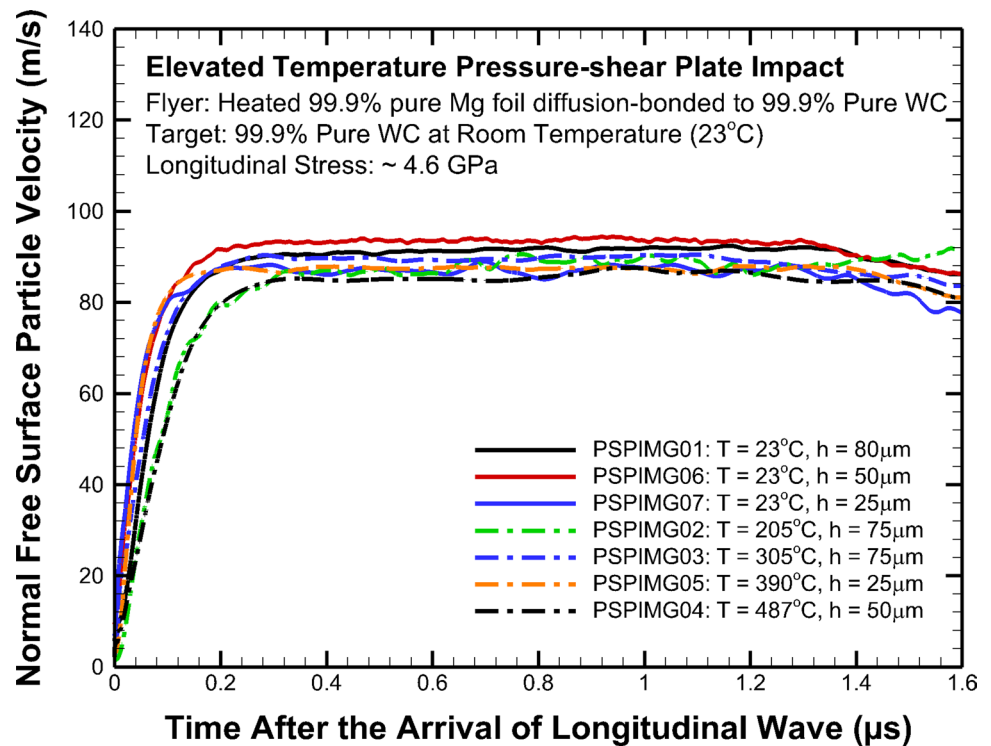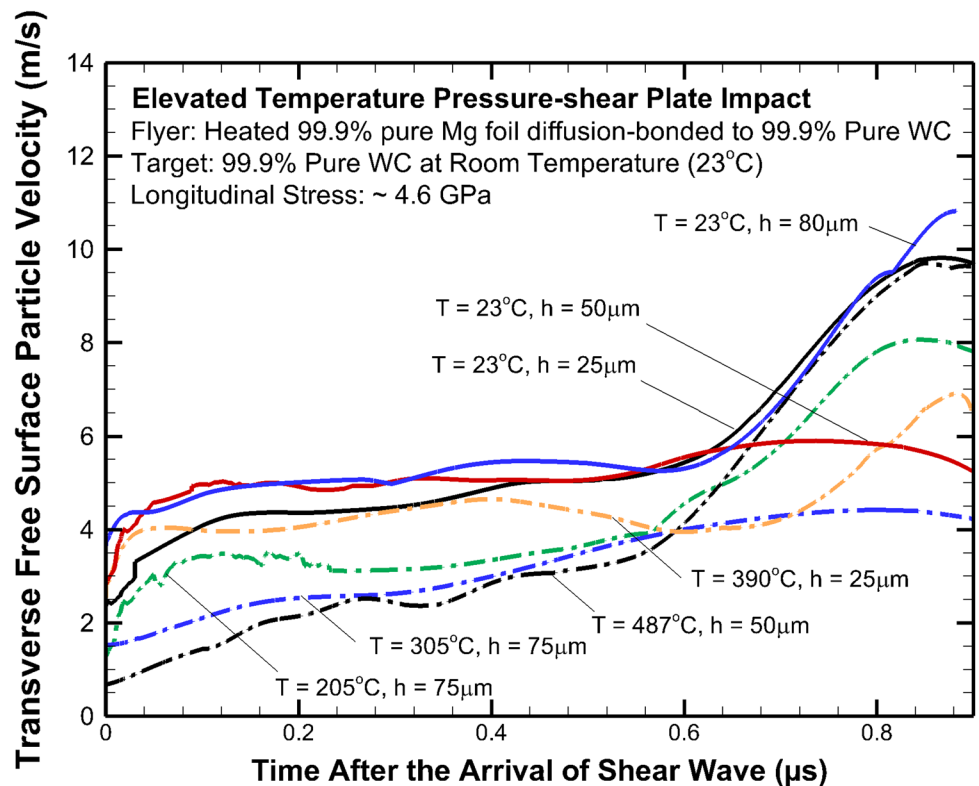

Fig. 6 Transverse free-surface velocities for pressure–shear experiments on 99.9% polycrys-talline pure magnesium. The time axis is shifted to coincide with the arrival of the shear wave at the free surface of the target plate

σ are $\sigma_1 = -p + \tau_{23}$, $\sigma_2 = -p$, and $\sigma_3 = -p - \tau_{23}$. It is to be noted that even though p and τ_{23} may vary with time, the corresponding eigenvectors remain fixed in space and only the magnitude of the eigenvalues change. Also, the

maximum resolved shear stress in the samples is given by $\tau_{max} = (\sigma_1 - \sigma_3)/2 = \tau_{23}$.

Accordingly, in a typical PSPI experiment, due to the oblique nature of impact the principal stress directions in the

sample do not align with the sample crystallographic directions and sample deformation cannot be predicted by simple CRSS analysis. Accordingly, low CRSS basal slip along with pyramidal slip (which has a higher CRSS when compared to basal slip) are the two most likely slip mechanisms to be activated. Moreover, extension twinning is expected to occur whenever the mismatch angle between the loading and sample crystallographic directions results in c-axis extension. Moreover, in the present experiments, once twinning is initiated it is expected to remain active until it completely consumes the sample grains.

The experimental shear stress vs. shear strain profiles obtained for the Mg samples are shown in Fig. 7. Also, shown in the figure are the plastic shearing rates in the samples. Shots PSPIMG01, PSPIMG06 and PSPIMG07 are conducted at room temperature, while Shots PSPIMG02, PSPIMG03, PSPIMG04 and PSPIMG05 are conducted at 205 °C, 305 °C, 487 °C, and 390 °C, respectively. In all experiments, the impact velocity is controlled to be ~ 100 m/s, such that, at impact, the WC back flyer plate and WC target plates remain elastic during the experiment. Under these impact conditions, the hydrostatic pressure developed in the sandwiched Mg samples is ~ 4.6 GPa. The sample shearing rates – which depend on the
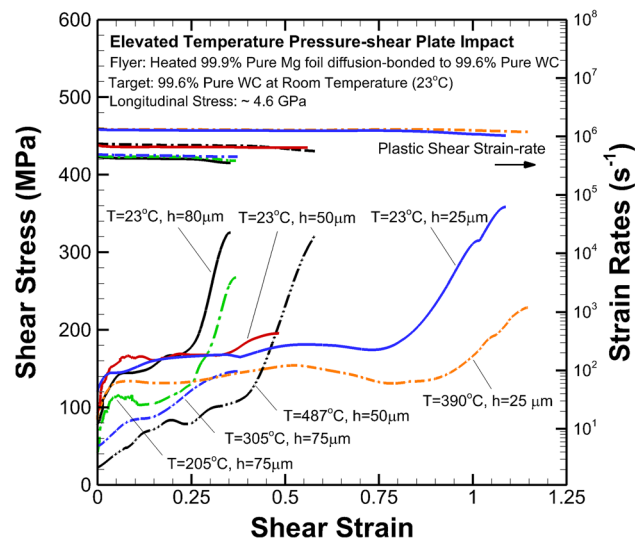

Fig. 7 Dynamic shearing resistance and shearing strain rates versus the accumulated shear stain for the PSPI experiments on 99.9% polycrystalline pure magnesium in the temperature range 23 °C to 487 °C. In all cases, the shear-stress versus shear-strain profiles show a three-stage deformation response, where, during Stage I the flow stress is observed to strain harden quickly and reach a plateau level; during Stage II the samples accumulate considerable shear strains at nearly a constant shear stress till the beginning of Stage III, where the flow stress is observed to increases rapidly with strain. Note that the beginning of Stage III is clearly visible in all experiments except for Shot PSPIMG03 (Temp = 305 °C and h = 75 μm, where it coincides with the arrival of the release wave from the lateral boundary of the specimen

shearing resistance of the samples, the impact velocity and the sample thickness – are controlled by strategically changing the sample thickness, *h*. Accordingly, samples with three different thicknesses are employed in the present study – 25 μm, 50 μm and 75–80 μm. In all cases, the dynamic shear-stress versus shear-strain profiles show a three-stage deformation response, where, during Stage I the flow stress is observed to strain harden quickly and reach a plateau level; during Stage II the samples accumulate considerable shear strains at nearly a constant shear stress level till the beginning of Stage III, where the flow stress is observed to increases rapidly with strain. Note that in Fig. 7, the beginning of Stage III is clearly visible for all experiments except for Shot PSPIMG03, where it coincides with the end of the window time for the experiment.

For the room temperature experiments, i.e., Shots PSPIMG01 (h = 80 μm), PSPIMG06 (h = 50 μm) and PSPIMG07 (h = 25 μm), the shear strain rates in the samples were 4.8×10^5 s^{-1}, 7.5×10^5 s^{-1}, and 1.045×10^6 s^{-1}, respectively. In these experiments, during Stage II deformation, the samples accumulate shear strain by dislocation-mediated slip and deformation twinning with little or no strain or strain-rate hardening, with the shear stress remaining constant at ~ 170 MPa. These relatively low CRSS deformation modes continue until deformation twinning is fully exhausted within individual grains of the Mg polycrystals, leading to reorientation of the parent crystal lattice and shifting deformation to relatively higher CRSS slip and twinning modes (as well as their interactions) at the beginning of Stage III. As strain accumulates during Stage III, non-basal slip along with contraction/double twinning are expected to be activated and become the dominant deformation mechanisms [33]. Additionally, dislocation slip is expected to be hindered due to twin boundary-dislocation interactions, thus increasing the shear stress required for the inelastic deformation to proceed [34].

It is to be noted that for Shot PSPIMG01, which is conducted at room temperature at a plastic shearing rate of ~ 4.8×10^5 s^{-1}, the upturn in stress (i.e., transition from Stage II to Stage III) occurs at a shear strain of ~ 0.25. However, for Shots PSPIMG06 and PSPIMG07 conducted at higher shear strain rates, the Stage II to Stage III transition is observed to shift to higher shear strains. For example, transition to Stage III occurs at a shear strain of 0.32 for Shot PSPIMG06 conducted at a shear strain rate of 7.5×10^5 s^{-1} and at 0.77 for Shot PSPIMG07 conducted at a strain rate of 1.45×10^6 s^{-1}. Also, a striking feature of deformation in Stage II is the absence of strain or strain-rate hardening even in the case of the two highest shear strain rate experiments, which show shear strains of 0.32 and 0.77, respectively, prior to reaching their transition points.

As discussed, earlier, inelastic deformation in polycrystalline HCP metals is understood to occur by both dislocation-mediated slip and twinning deformation. Accordingly, in the Stage II deformation regime, inelastic deformation proceeds with minimal strain hardening until twinning exhausts itself by engulfing entire sample grain(s) and shifting deformation to higher CRSS modes as it transitions to Stage III. The marked increase in strain at the transition point (i.e., the strain at twin exhaustion) observed in the highest shear strain rate PSPI experiment (conducted at room and 390 °C test temperatures with h = 25 μ m), indicates that at increasing strain rates, dislocation mediated and "other" inelastic deformation mechanism(s) accompanying twinning delay transition to Stage III. We believe these "other" inelastic deformation modes to be a combination of grain boundary sliding accommodated by grain rotation, similar to what has been observed during room and moderate temperature cold rolling processes in polycrystalline pure Mg. Also, since both extension twinning and these geometric softening deformation mode(s) are understood to be only weakly sensitive to strain and strain-rate hardening [3, 5], the shear stress vs shear strain profiles in this deformation regime remain essentially flat.

Further insights into the kinetics of twinning and dislocation-mediated plastic slip mechanisms under the combined pressure and shear loading is gained by studying the transverse particle velocity versus time profiles, shown in Fig. 6. Focusing on the room temperature experiments (i.e., Shots PSPIMG01 (h = 80 μ m), PSPIMG06 (h = 50 μ m) and PSPIMG07 (h = 25 μ m), with sample shear strain rates 4.8×10^5 s^{-1}, 7.5×10^5 s^{-1}, and 1.045×10^6 s^{-1}, respectively), we note that the time at which the upturn in shear stress (transition from Stage II to Stage III) occurs is ~ 550 ns in all the three shots after the arrival of the shear wave at the free surface of the target. This result is intriguing considering the very different sample shear strain rates in the three experiments and suggests that the average rate of growth of twin volume fraction is nearly the same in the three experiments.

Since, during the high rate shearing deformation dislocation-mediated plastic flow is accompanied by twinning, the total sample plastic shear strain rate, $\dot{\gamma}_{23}^p$, in the sample in the shearing direction can be written as a sum of dislocation mediated shear rate, $\dot{\gamma}_{\perp}$ and twin mediated shear rate, $\dot{\gamma}_{Tw}$, i.e.

$$\dot{\gamma}_{23}^p = \dot{\gamma}_{\perp} + \dot{\gamma}_{Tw} \tag{3}$$

The second term on the right-hand side of Eq. (3) can be further expressed as $\dot{\gamma}_{Tw} = \dot{f}_{Tw}\gamma_{Tw}$, where f_{Tw} is the volume fraction of twins, and γ_{Tw} is the twinning shear defined as the shear strain associated with the lattice orientation.

Then, from Eq. (3), it follows that

$$\dot{f}_{Tw} \leq \frac{\dot{\gamma}_{23}^p}{\gamma_{Tw}} \tag{4}$$

Taking the twinning shear $\gamma_{Tw} = 0.129$ [35] and using Eq. (4) along with the total shear strain rate obtained in the lowest shear strain rate PSPI experiment (Shot PSPIMG01 – 4.8×10^5 s^{-1} at room temperature), suggests a limiting twin volume fraction growth rate of 3.72×10^6 s^{-1}, which cannot be exceeded in the present PSPI experiments. It is interesting to note that this limiting twin volume fraction rate is approximately two orders of magnitude greater than $\sim 2.1 \times 10^4$ s^{-1}, which was estimated by Kannan et al. [36] at strain rates of ~ 2000s^{-1} from their study on single crystal Mg using the SHPB.

Next, to estimate the critical time for exhaustion of twinning during pressure-shear loading, we use the approach developed by Johnson et al. [37], where the expression for volume fraction of twinning as a function of time was obtained as

$$V_{ftw}(t) = \left[\frac{1}{T_R} \int_0^t \left(\frac{\tau}{\tau_o} - 1 \right) dt \right]^m if \tau > \tau_0 \tag{5}$$

The model parameters in Eq. (5) were determined from experiments on single crystal Mg by Renganathan et al. [35] as $T_R = 2\mu s$, $\tau_0 = 6$MPa and m = 3.

Taking $\tau = 165$MPa during Stage II deformation for Shots PSPIMG01, PSPIMG06 and PSPIMG07, the time for twin exhaustion, t_{exh}, can be estimated using Eq. (5) as

$$t_{exh} = \frac{T_r}{\left(\frac{\tau}{\tau_o} - 1 \right)} = 75.4\text{ns} \tag{6}$$

This result suggests that in the three room-temperature PSPI experiments, twinning is expected to be exhausted very early (after 75.4 ns) in the loading process. The corresponding twin volume fraction rate is estimated to be 13.2×10^6 s^{-1}, which is 3.5 times higher than the limiting twin growth volume fraction rate determined by Eq. (4). It must be noted that the parameters used in Eq. (5) were calibrated using data from normal plate impact experiments on Mg single crystals impacted along the < c > and < a > directions at room temperature, and probably need to be re-calibrated for the current PSPI experiments on polycrystalline Mg. It is also equally probable that the model parameters are applicable to the present PSPI experiments, but the predicted extremely high twin volume fraction rates are not sustainable and result in local dynamic processes that can hinder (quench) competing twin growth during the dynamic shearing process, leading to saturation of the effective twin volume fraction growth rate at a lower level.

Using the limiting strain rate estimated from Eq. (4), instead, to obtain the twin exhaust time establishes the

lower time limit for twin exhaustion as $t_{exh} \geq 268.8 ns$. Based on the experimental profiles shown in Fig. 6, t_{exh} can be estimated to be ~550 ns for the three room-temperature experiments. Since at twin exhaustion the twin volume fraction is unity, an ***average*** twin volume fraction growth rate of 1.8×10^6 s^{-1} is estimated. Also, since twinning upto twin exhaustion accounts for ~0.129 shear strain, the remaining inelastic deformation has to be accommodated by other inelastic mechanisms, such as dislocation mediated slip, grain boundary sliding, etc. This is especially applicable to Shot PSPIMG07, conducted at a shear strain rate of 1.045×10^6 s^{-1}, where nearly 0.63 shear strain has to be accommodated by inelastic slip processes other than twinning.

Another important result inferred from the elevated temperatures PSPI experiments, i.e., Shots PSPIMG02 (205 °C, 4.8×10^5 s^{-1}), PSPIMG03 (305 °C, 4.8×10^5 s^{-1}) and PSPIMG04 (487 °C, 7.5×10^5 s^{-1}), is that the shearing resistance of the samples decrease progressively as the test temperatures are increased from room to 487 °C. This behavior is to be expected for most polycrystalline metals in view of the lowering of dislocation mobility barrier(s) for thermally activated slip as the test temperatures are increased. Also, unlike in the case for room temperature experiments, at elevated temperatures significant strain hardening is observed during the Stage I and II deformation, all the way up to the Stage III transition point. Note that since extension twinning is understood to be temperature insensitive [38] and basal slip to be only weakly sensitive to temperature [3], the observed flow behavior in Stages I and II requires other higher CRSS dislocation-mediated slip deformation modes, such as, non-basal slip to sustain the shearing deformation. The activation of this non-basal slip is believed to be responsible for the observed strain hardening in Stages I and II during the deformation process.

Besides strain hardening, significant strain-rate hardening is also observed at elevated temperatures in Stages I and II. For example, for Shot PSPIMG05 (strain-rate ~1.045×10^6/s and test temperature of 390 °C), the shear stress level in Stage II (~142 MPa) is higher than those measured for Shots PSPIMG02 and PSPIMG03 conducted at lower test temperatures of 205 °C and 305 °C, respectively, and at much lower shear strain rates, while being lower than those measured at room temperature for Shots PSPIMG01, PSPIMG06, and PSPIMG07.

In addition, at elevated temperatures, a consistent shift in Stage II to Stage III transition point is observed as the test temperatures (and plastic shearing rates) are increased, with transition occurring at ~0.25, 0.33, 0.37, and 0.9 shear strains for Shots PSPIMG02 (205 °C, 4.8×10^5 s^{-1}), PSPIMG03 (305 °C, 4.8×10^5 s^{-1}), PSPIMG04 (487 °C, 7.5×10^5 s^{-1}) and PSPIMG05 (390 °C, 1.045×10^6 s^{-1}), respectively. It is interesting to note from Fig. 6 that the twin

exhaustion times for these elevated temperature experiments are estimated to be $t_{exh} \sim 550$ °C, which is similar to those observed for room temperature experiments. As discussed earlier, the shift in transition point can again be attributed to the saturation of the twin volume fraction growth rate at 1.8×10^6 s^{-1}, which requires increased dislocation slip along with the possibility of geometric strain softening to accompany twinning during the deformation process, thus shifting the Stage II to III transition to higher shear strain levels. This is an important result and states that during high rate shearing deformation of polycrystalline pure Mg, the average twin volume fraction growth rate is both strain rate and temperature insensitive and remains nearly constant in all experiments under conditions applicable to the present study.

Estimation of Maximum Sample Temperature Rise in the Mg samples

The Helmholtz free energy, ψ, is defined as the energy per unit mass available to do work at constant temperature, i.e.,

$$\psi = e - \eta T, \tag{7}$$

where e is the internal energy per unit mass, η is the entropy per unit mass and T is the temperature.

Without loss of generality, the Helmholtz free energy can be taken as a state function of the elastic Green–Lagrange strain, E^e, temperature, T, and a set of internal state variables $\xi_1, \xi_2 \ldots \xi_k$, where each ξ_i may be a tensor, i.e.,

$$\psi = \hat{\psi}\left(E^e, T, \xi_1, \xi_2 \ldots \xi_k\right). \tag{8}$$

For estimating the *maximum* temperature rise in the Mg samples, we consider an adiabatic deformation process with all heat generated by elastic–plastic work going solely to increasing the sample temperature with no energy being stored within the sample., i.e., the Taylor Quinney coefficient is one.

Under these conditions, for isotropic materials, the change in sample temperature can be expressed as [24, 39]

$$dT = \frac{\left(\overline{\tau} d\overline{\gamma}^p + \alpha T dP\right)}{\overline{\rho}\,\overline{C}_E}. \tag{9}$$

In Eq. (9), $\overline{\tau}$ is the effective shear stress, $\overline{\gamma}^p$ is the equivalent plastic shear strain, $\overline{\tau} d\overline{\gamma}_p$ is the plastic work, $\overline{C}_E$ is the specific heat at constant strain, and α is the volumetric coefficient of thermal expansion. The first term on the RHS contributes to the temperature rise due to the plastic work in the sample while the second term is the contribution from the change in pressure, P.

The pressure, effective shear stress and the equivalent plastic shear strain can be calculated from measurements taken during a typical pressure-shear experiment. The density $\bar{\rho}$, the coefficient of thermal expansion α, and the specific heat capacity, $\overline{C}_E$, are all known for polycrystalline pure Mg at ambient conditions. Also, since the applied pressure in the present experiments is modest, we consider variations of all thermodynamic quantities of interest to be only a function of temperature.

The linear thermal expansion coefficient α (10^{-6}/K) of commercially pure polycrystalline magnesium at any temperature T (^{o}C) is described by the relationship α(T) = 24.66 + 0.01952T for temperatures in the range 20 °C < T < 500 °C [40]; this relationship can also be used to estimate the density of magnesium foil samples at the various test temperatures using $\rho(T) = \frac{\bar{\rho}}{\left(1+\alpha\left(T-T_o\right)^3\right)}$, where $\bar{\rho}$ is 1.740 g/cm^3 at ambient conditions. Moreover, the specific heat capacity of magnesium C_E J/(K-mole) as a function of temperature T (^{o}C) can be described, within sufficient accuracy, by the relationship C_E(T) = 24.5337208 +1.0704764 $\times 10^{-2}$T − 0.4803232 $\times 10^{-8}$T^2 [41].

The melting temperature of pure Mg is taken to increase proportionally with pressure P, as [42]

$$T_m(P) \approx -0.6212P^2 + 63.04P + 925.93, \quad (10)$$

where, P is estimated to be equal to the compressive stress $\sigma_{33}(t)$ and can be estimated from the measurement of the normal component of the free surface particle velocity $u_{fs}(t)$., as

$$P \approx \sigma_{33}(t) = \frac{\left(\rho C_L\right)_T}{2} u_{fs}(t). \quad (11)$$

Since the WC target plate remains elastic at room temperature during the experiments, the longitudinal impedance $\left(\rho C_L\right)_T$ is taken to be constant in Eq. (11).

In estimating the temperature rise from the measured normal and transverse wave profiles, the normal stress and shear stress versus time plots are time-shifted in accordance such that the sample is subjected to both components of stress starting at impact (t = 0). The temperature increment and temperature dependent material properties (e.g., density, specific heat capacity, linear thermal expansion coefficient) are updated at each time step. The sample temperature (solid lines), pressure dependent sample melt temperature (dashed lines), and the sample temperature as a percentage of the melting temperate (dashed-dot lines), are presented in Fig. 8 for Shots PSPIMG01, PSPIMG02, PSPIMG04 and PSPIMG05. The estimated temperature rise in the samples for these experiments under adiabatic conditions are ~ 38 °C, 34 °C, 106 °C, and 68 °C for the 23 °C (PSPIMG01), 205 °C (PSPIMG02), 390 ˚C (PSPIMG05) and 487 °C (PSPIMG04)

Shots, respectively. Shot PSPIMG05 shows the largest increase in sample temperature because of the relatively large plastic deformation that occurs in the sample during the high-rate shearing, which greatly contributes to the plastic work.

The T/T$_m$ ratio for pure Mg at impact is observed to drop off quickly during the initial phase of the shearing deformation due to the large increase in the melt temperatures (~ 125 °C), but then increases with deformation as the plastic work is converted to heat. The final sample temperatures for PSPIMG01, PSPIMG02, PSPIMG05, PSPIMG04 are estimated to be 61 °C, 249 °C, 496 °C, and 555 °C with T/T$_m$ of ~ 6%, 28%, and 53%, 60%, respectively, showing that the sample remain in its solid state during all experiments conducted in the present study.

Summary

In the present study, a series of elevated temperature pressure–shear plate impact experiments are conducted on polycrystalline 99.9% pure magnesium foil samples at ultra–high strain rates (10^5/s–10^6/s) and test temperatures of 23 °C, 205 °C, 305 °C, 390 °C and 487 °C. In all cases, the dynamic stress–strain profiles show a three-stage deformation process where at the transition from Stage II to Stage III the shear stress increases rapidly with strain. At room temperature, during Stages I and II, the sample flow stress shows little or no strain- or strain-rate hardening, with the shear stresses remaining at a level of ~ 170 MPa. This lack of hardening is attributed to the presence of geometric strain softening deformation modes and twinning that can accommodate inelastic strains during the deformation process. Transition to the Stage III deformation regime is understood to mark the exhaustion of twinning during Stage II, when the twinned grains reorient themselves shifting deformation to higher CRSS slip and twinning modes [10, 11, 19]. It is interesting to note that, while for the thicker foil sample (with shear strain rate ~ 4.8×10^5 s^{-1}) the upturn in shear stress (transition from Stage II to Stage III) occurs at a strain of ~ 0.25, which shifts to the right as the strain rates are increased, i.e. the strain at the transition point increases to 0.32 as the strain rates are increased to 7.5×10^5 s^{-1} in the 50 μm thick sample, and to 0.77 at 1.45×10^6 s^{-1} in the 25 μm thick foil. The shearing resistance of the samples decreases progressively as the test temperatures are increased from room to 487 °C. This behavior is to be expected in most polycrystalline metals in view of the lowering of barrier(s) for thermally activated slip with increase in sample temperatures. In addition, contrary to the room temperature experiments, at elevated temperatures, significant strain hardening is observed during in the Stage I and II deformation regimes all the way to the transition point. Since extension twinning is understood to be nearly

Fig. 8 Temperature Ts in the magnesium samples as a function of time after impact due to the adiabatic conversion of elastic–plastic work to heat along with the pressure dependent melting temperature, Tm.
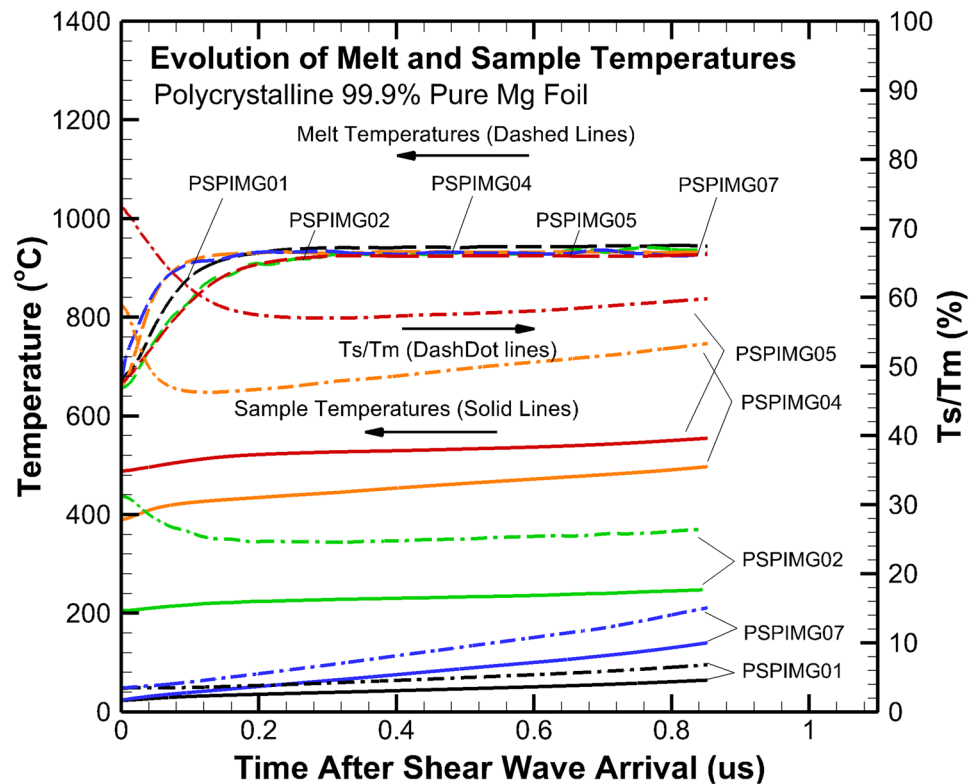
temperature insensitive and basal slip to be only weakly sensitive to temperature [11], the observed hardening behavior suggests that other higher CRSS deformation modes, such as non-basal slip and contraction/double twinning, are activated as the test temperatures are increased. Besides higher strain hardening, increased rate sensitivity at ultra–high strain rates and elevated temperatures is observed in the sample. For example, at a sample strain-rate of $\sim 1.45 \times 10^6$/s, the stress levels in Stages I and II at 390 °C is higher than those obtained at 205 °C and 305 °C, but still lower than those obtained in the room temperature experiments. This response is in contrast to the rate sensitivity observed in the room temperature PSPI experiments, where the stress levels in Stages I and II are all very similar at markedly different strain rates. Moreover, a limiting twin volume fraction growth rate of 1.8×10^6 s^{-1} is identified in the study, which is found to be both strain rate and temperature independent and remains constant in all experiments under conditions applicable to the present study.

To the best of the authors knowledge the results presented herein are the first on dynamic shearing resistance of polycrystalline Mg at elevated temperatures (up to 487 °C) and ultra–high shearing rates (in the range 10^5 to 10^6 s^{-1}). The only other studies on dynamic shearing resistance of polycrystalline Mg and its alloys was conducted by Zhao et al. [43] and Ravindran et al. [44], where they reported high strain rate pressure–shear plate impact experiments at strain rates of up to $\sim 10^5$/s *at room*

temperature and shear strains of only ~ 0.25, which are a factor of four lower than those achieved in the present study.

References

1. Kaiser F, Letzig D, Bohlen J, Styczynski A, Hartig C, Kainer KU (2003) Anisotropic properties of magnesium sheet AZ31. Materials science forum: magnesium alloys 2003, editors. Y. Kojima, T. Aizawa, K. Higashi, S. Kamados. Trans Tech Publ. pp. 315–320.
2. Tucker MT, Horstemeyer MF, Gullett PM, El Kadiri H, Whittington WR (2009) Anisotropic effects on the strain rate dependence of a wrought magnesium alloy. Scripta Mater 60(3):182–185
3. Chapuis A, Driver JH (2011) Temperature dependency of slip and twinning in plane strain compressed magnesium single crystals. Acta Mater 59(5):1986–1994
4. Jain A, Agnew SR (2007) Modeling the temperature dependent effect of twinning on the behavior of magnesium alloy AZ31B sheet. Mater Sci Eng, A 462(1):29–36
5. Dudamell NV, Ulacia I, Galvez F, Yi S, Bohlen J, Letzig D, Hurtado I, Perez-Prado MT (2011) Twinning and grain subdivision

during dynamic deformation of a Mg AZ31 sheet alloy at room temperature. Acta Mater 59(18):6949–6962

6. Klimanek P, Pötzsch A (2002) Microstructure evolution under compressive plastic deformation of magnesium at different temperatures and strain rates. Mater Sci Eng, A 324(1):145–150

7. Choi HJ, Kim Y, Shin JH, Bae DH (2010) Deformation behavior of magnesium in the grain size spectrum from nano-to micrometer. Mater Sci Eng, A 527(6):1565–1570

8. Somekawa H, Mukai T (2005) Effect of grain refinement on fracture toughness in extruded pure magnesium. Scripta Mater 53(9):1059–1064

9. Jeong J, Alfreider M, Konetschnik R, Kiener D, Oh SH (2018) In-situ TEM observation of 101⁻ 2 twin-dominated deformation of Mg pillars: twinning mechanism, size effects and rate dependency. Acta Mater 158:407–421

10. Barnett MR (2007) Twinning and the ductility of magnesium alloys Part II. "Contraction" twins. Mater Sci Eng, A 464:8–16

11. Barnett MR (2007) Twinning and the ductility of magnesium alloys Part I: "Tension" twins. Mater Sci Eng, A 464:1–7

12. Beyerlein IJ, McCabe RJ, Tomé CN (2011) Effect of microstructure on the nucleation of deformation twins in polycrystalline high-purity magnesium: a multi-scale modeling study. J Mech Phys Solids 59(5):988–1003

13. Beyerlein IJ, McCabe R, Tome C (2011) Stochastic processes of 10–12 deformation twinning in hexagonal close-packed polycrystalline zirconium and magnesium. Int J Multiscale Comput Eng 9(4):459–480

14. Zhang J, Joshi SP (2012) Phenomenological crystal plasticity modeling and detailed micromechanical investigations of pure magnesium. J Mech Phy Solids 60(5):945–972

15. Knezevic M, Levinson A, Harris R, Mishra RK, Doherty RD, Kalidindi SR (2010) Deformation twinning in AZ31: Influence on strain hardening and texture evolution. Acta Mater 58(19):6230–6242

16. Kumar A, Hauser F, Dorn J (1968) Viscous drag on dislocations in aluminum at high strain rates. Acta Metall 16(9):1189–1197

17. Regazzoni G, Kocks UF, Follansbee PS (1987) Dislocation kinetics at high strain rates. Acta Metall 35(12):2865–2875

18. Zuanetti B, Wang T, Prakash V (2017) A novel approach for plate impact experiments to determine the dynamic behavior of materials under extreme conditions. J Dynamic Behav Mater 3:64–75

19. Wang T, Zuanetti B, Prakash V (2017) Shock response of commercial purity polycrystalline magnesium under uniaxial strain at elevated temperatures. J Dynamic Behav Mater 3(4):497–509

20. Clifton RJ, Klopp RW (1985) Pressure Shear Plate Impact Testing. Mechanical Testing, Metals Handbook, Ninth Edition (8 ed.), ASM, Metals Park, pp.230–239

21. Sunny G, Yuan F, Prakash V, Lewandowski JJ (2008) Effect of high strain rates on peak stress in a Zr-based bulk metallic glass. J Appl Phys 104:093522

22. Yuan FP, Prakash V, Lewandowski JJ (2009) Spall strength of a zirconium-based bulk metallic glass under shock-induced compression-and-shear loading. Mech Mater 41(7):886–897

23. Tsai L, Prakash V (2005) Structure of weak shock waves in 2-D layered material systems. Int J Solids Struct 42(2):727–750

24. Zuanetti B, Luscher DJ, Ramos K, Bolme CA, Prakash V (2021) Dynamic flow stress of pure polycrystalline aluminum: pressure-shear plate impact experiments and extension of dislocation-based modeling to large strains. J Mech Phys Solids 146(104185):1–30

25. Liou NS, Okada M, Prakash V (2004) Formation of molten metal films during metal-on-metal slip under extreme interfacial conditions. J Mech Phys Solids 52(9):2025–2056

26. Prakash V, Mehta N (2012) Uniaxial compression and combined compression-and-shear response of amorphous polycarbonate at high loading rates. Polym Eng Sci 52(6):1217–1231

27. Yuan F, Prakash V, Lewandowski JJ (2010) Shear yield and flow behavior of a Zirconium-based bulk metallic glass. Mech Mater 42(3):248–255

28. Okada M, Liou NS, Prakash V (2002) Dynamic shearing resistance of molten metal films at high pressures. Exp Mech 42(2):161–171

29. Zuanetti B, Wang T, Prakash V (2017) A compact fiber-optics based heterodyne combined normal and transverse displacement interferometer. Rev Sci Inst 88:033108

30. Prakash V, Clifton RJ (1992) Experimental and Analytical Investigations of Dynamic Fracture under Conditions of Plane-Strain. Fracture Mechanics: Twenty Second Symposium (vol. 1) ASTM STP 1131 ed.), American Society of Testing Materials, Philadelphia, PA, pp.412–444

31. Zuanetti B, Wang T, Prakash V (2019) Plate impact investigation of the dynamic response of commercial tungsten carbide under shock-induced compression and combined compression-and-shear loading. Int J Impact Eng 131:200–208

32. Wang T, Prakash V (2021) Inelastic deformation mechanisms in shock compressed polycrystalline pure magnesium at temperatures approaching melt. J Dynamic Behav Mater 7:279–293

33. Chang Y (2016) A continnum model for slip-twinning interactions in magnesium and magnesium alloys, Doctor of Philosophy, California Institute of Technology, Pasadena, CA.

34. Levinson AJ (2012) The role of deformation twinning on strain hardening and recrystallization in magnesium alloy AZ31, PhD Dissertation, Drexel University,

35. Renganathan P, Winey JM, Gupta YM (2017) Shock compression and release of a-axis magnesium single crystals: Anisotropy and time dependent inelastic response. J. Appl Phys 121:035901

36. Kannan V, Hazeli K, Ramesh KT (2018) The mechanics of dynamic twinning in single crystal magnesium. J Mech Phys Solids 120:154–178

37. Johnson JN, Rohde RW (1971) Dynamic deformation twinning in shock-loaded iron. J Appl Phys 42(11):4171–4182

38. Liu Q, Roy A, Silberschmidt VV (2017) Temperature-dependent crystal-plasticity model for magnesium: a bottom-up approach. Mech Mater 113:44–56

39. Luscher DJ, Buechler MA, Walters DJ, Bolme CA, Ramo KJ (2018) On computing the evolution of temperature for materials under dynamic loading. Int J Plast 111:188–210

40. Hidnert P, Sweeney WT (1928) Thermal expansion of magnesium and some of its alloys. Bur Stan J Res 1:771–792

41. Poppema TJ, Jaeger FM (1935) The exact measurement of the specific heats of solid substances at higher temperatures. XIX. The specific heats of zinc, magnesium and their binary afloy: MgZn2. Proceedings Royal Acad. XXXVIII 510–520.

42. Errandonea D (2010) The melting curve of ten metals up to 12 GPa and 1600 K. J Appl Phys 108(3):033517

43. Zhao M, Kannan V, Ramesh KT (2018) The dynamic plasticity and dynamic failure of a magnesium alloy under multiaxial loading. Acta Mater 154:124–136

44. Ravindran S, Lovinger Z, Gandhi V, Mello M, Ravichandran G (2020) Strength of magnesium at high pressures and strain rates. Extreme Mech Lett 41:1044